PNAS RESEARCH ARTICLE | PHYSICS

Evidence of intertwined pair density and charge density wave orders in UTe_2

Zhen Zhu[a], Yudi Huang[a], Julian May-Mann[b], Kaiming Liu[a], Zheyu Wu[c], Shanta R. Saha[d], Johnpierre Paglione[d,e], Alexander G. Eaton[c], Andrej Cabala[f], Michal Vališka[f], Eduardo Fradkin[a,g,1], and Vidya Madhavan[a,e,1]

Affiliations are included on p. 8.

Contributed by Eduardo Fradkin; received February 3, 2026; accepted June 17, 2026; reviewed by Daniel Agterberg, Abhay N. Pasupathy, and Ali Yazdani

The strongly correlated spin-triplet superconductor UTe_2 hosts an unusual magnetic-field-sensitive charge density wave (CDW) phase, positioning it as a compelling system for studying intertwined electronic orders. A central challenge is determining whether the observed charge modulations arise from a triplet pair density wave (PDW) order and, if so, how the anisotropic magnetic field response of triplet superconductivity is manifested in the CDW response. Here, using a scanning tunneling microscope equipped with a vector magnetic field, we systematically investigate the evolution and interrelation of distinct CDW orders. Complementing the previously identified incommensurate CDW peaks ($q_{i=1,2,3}$), we resolve an additional set of nondispersive modulations ($p_{i=1,2,3}$ and $h_{1,2}$) with distinct temperature and magnetic field dependencies. The p_i CDW peaks vanish near T_c, while the q_i peaks survive well above T_c but are progressively suppressed by magnetic field in an anisotropic manner. The critical fields of the q_i peaks mirror the directional hierarchy of H_{c2}, which suggests a PDW is present above the bulk T_c. This is consistent with a Landau free-energy picture where PDWs with wavevectors p_i form above the bulk T_c, leading to composite CDW orders with wavevector q_i. Below T_c, the coupling of PDWs and uniform superconductivity leads to the p_i CDWs. Together, these findings establish UTe_2 as a rare platform where both the parent PDW and descendant orders are directly resolved, enabling access to both the fundamental and emergent manifestations of PDW physics.

superconductivity | charge density wave | pair density wave | intertwined orders | heavy fermions

Significance

Correlated, spin-triplet superconductors are promising platforms for realizing emergent phases. Under certain conditions, the superconducting order can intertwine with spatially modulated superconductivity known as a pair density wave (PDW). In the triplet superconductor UTe_2, our experiments reveal a multicomponent charge density wave (CDW) order with 1Q peaks that disappear near the bulk superconducting T_c, while the 2Q peaks persist to higher temperatures. Magnetic-field measurements together with a Ginzburg–Landau analysis show that the 1Q CDW peaks likely originate from a PDW coupled to uniform superconductivity. The natural and simplest explanation of the state observed above T_c is a PDW superconducting state, at least on the sample surface. These findings establish a platform for exploring intertwined triplet superconductivity and PDW order.

Intertwined electronic orders represent a central theme in correlated quantum materials, where multiple orders like electronic nematicity, superconductivity, charge density wave (CDW), and spin density wave (SDW) do not merely coexist or compete but arise from a common microscopic origin (1–4). Unlike conventional competition or coexistence between different phases, intertwined states often emerge in the overlapping regions of the phase diagram, exhibit comparable onset temperatures, and are linked by mutual coupling and symmetry constraints. A prominent manifestation of this paradigm is the pair density wave (PDW) state, a superconducting phase with a spatially modulated order parameter, which intertwines superconductivity and CDW order.

Accumulating experimental evidence supports the presence of PDW states in a variety of correlated systems, including cuprates (5–7), transition metal dichalcogenides (8–10), kagome metals (11, 12), and iron-based superconductors (13, 14). In particular, the heavy-fermion compound UTe_2 has emerged as a promising platform for realizing this exotic order. UTe_2 is a spin-triplet superconductor with an unconventional pairing mechanism and an extremely large and anisotropic upper critical field ($H^b_{c2} > H^c_{c2} > H^a_{c2}$), reaching well beyond the Pauli limit (15). Early-stage UTe_2 crystals exhibit superconductivity with $T_c \approx 1.6$ K, field-reinforced superconductivity beyond 30 T (16), and signature of chiral spin-triplet pairing (17). Next-generation crystals grown by molten flux methods exhibit an enhanced $T_c \approx 2.1$ K (18–20). Benefiting from their ultrahigh residual resistivity ratios and exceptional crystallinity, these samples provide an ideal platform that is less susceptible to extrinsic effects and point to a strengthened spin-triplet pairing component, as evidenced by higher T_c, increased H_{c2} along all three crystallographic axes, and an expanded high-field superconducting phase (21).

An unusual incommensurate CDW order (q_i, $i = 1, 2, 3$) was observed in the early-stage UTe_2 samples, which melts near H_{c2}, suggesting that the observed charge modulations arise from PDWs (22–24). In this picture, spin-triplet PDWs with momentum q_i, together with uniform spin-triplet superconductivity, naturally produce CDWs at momentum q_i. This framework accounts for the magnetic-field sensitivity of the CDWs through vortex-induced dislocations. However, several puzzles remain. For instance, if the CDWs are generated by

Author contributions: Z.Z. and V.M. designed research; Z.Z., Y.H., and K.L. performed research; Z.W., S.R.S., J.P., A.G.E., A.C., and M.V. contributed new reagents/analytic tools; Z.Z., Y.H., and V.M. analyzed data; J.M.-M. and E.F. provided theoretical input on the interpretation of the data; and Z.Z., J.M.-M., E.F., and V.M. wrote the paper.

Reviewers: D.A., University of Wisconsin-Milwaukee College of Letters and Science; A.N.P., Columbia University; and A.Y., Princeton University.

The authors declare no competing interest.

[1]To whom correspondence may be addressed. Email: efradkin@illinois.edu or vm1@illinois.edu.

This article contains supporting information online at https://www.pnas.org/lookup/suppl/doi:10.1073/pnas.2602117123/-/DCSupplemental.

Published July 15, 2026.

the combination of PDWs and uniform superconductivity, they would be expected to vanish once uniform superconductivity is lost. Yet the field-sensitive CDWs persist well above T_c up to ~5 K.

Recent studies have offered new insights, but the interpretation of the data has varied across the community. The common feature between groups is the presence of spectral signatures with reduced wavevectors, distinct from the previously known CDW order (25–27) (here labeled as h_1, h_2, p_1, p_2, p_3). Peaks at p_1, p_2, and p_3 (henceforth referred to as p_i) were observed in applied magnetic fields at 30 mK temperatures and attributed to primitive CDW components (25) owing to their commensurate relationship with q_1, q_2, and q_3, as each exhibits a wavevector of half the corresponding q_i. On the other hand, in different studies, peaks at h_1, h_2 and p_3 were seen at energies within the superconducting gap and attributed to quasiparticle interference (QPI) from in-gap states along the nodal direction (26, 27). The microscopic origin of these multiple momentum space signatures and their relationship to the bulk homogeneous superconducting state is thus an important open question which has direct consequences for our understanding of the superconducting state.

In this work, we address these questions by studying next-generation UTe_2 samples ($T_c \approx 2.1$ K, *SI Appendix*, Fig. S1) using a vector-magnetic-field scanning tunneling microscope (STM). With this capability, we systematically investigate the temperature and field evolution of the established and newly emergent CDW orders in UTe_2. The $h_{1,2}$ and p_3 vectors are intrinsic to the zero-field state, whereas p_1 and p_2 are induced by applied magnetic fields. Energy-dependent *dI/dV* maps establish that the $h_{1,2}$ and p_3 peaks, with wavevectors comparable to previous studies (26, 27), remain nondispersive at energies well above the superconducting gap, confirming their classification as CDW modulations. We further show that the zero-field p_3 and field-induced $p_{1,2}$ peaks possess wavevectors that are half of q_3 and $q_{1,2}$. While this wavevector relationship may suggest that q_i is a harmonic of p_i (25), the differing onset temperatures are incompatible with a simple harmonic interpretation. Notably, the p_2 and p_3 peaks are strongly coupled to superconductivity and vanish near the bulk T_c, while the q_i peaks survive to higher temperatures. Although the p_1 peak temperature dependence was not tracked, it is related by symmetry to the other peaks and is expected to show a similar temperature dependence as p_2 and p_3.

Our vector magnetic field response of the peaks conducted both below and above the superconducting T_c uncover additional clues to their origin. Taken together and in combination with Landau free energy, our data provide a refined explanation for both the newly observed and previously identified CDW peaks in terms of spin-triplet PDWs with wavevectors p_i and uniform spin triplet superconductivity. In the new explanation, the PDWs have wavevectors p_i. The q_i CDWs arise purely from the PDWs, and the p_i CDWs arise from the combination of PDW and uniform superconductivity.[*] This explains why the p_i peaks only show up in the STM data below the bulk T_c, and accounts for the hierarchical magnetic field destruction of the q_i CDWs at 4.2 K. The spin-triplet nature of the PDW and uniform superconductivity can also account for the fact that p_1 and p_2 are induced by a magnetic field.

UTe_2 crystallizes in an orthorhombic structure (space group Immm), in which Te atoms form chains along the crystallographic *b* axis, while U dimers oriented along the *c* axis assemble into chains extending along the *a* axis (Fig. 1 *A* and *B*). STM measurement on a cleaved surface of UTe_2 reveals quasi-one-dimensional Te chains along the *a* axis (Fig. 1*C*), consistent with previous studies (17, 23). Each U atom is coordinated by two inequivalent tellurium atoms, Te1 (light blue) and Te2 (dark blue). Owing to the centrosymmetric nature of the bulk structure, UTe_2 can cleave along either the (01-1) or (011) surface (17, 23), leading to surface terminations with Te1 and Te2 chains swapping their relative positions. On both cleavage surfaces, the Te1 chains appear slightly elevated compared to the Te2 chains, serving as a distinguishing feature (17). Based on the spatial arrangement of Te1 and Te2 atoms observed in the high-resolution topography (*Inset* of Fig. 1*C*) and following established criteria, we tentatively identify the cleavage plane in this study as (01-1). This identification in turn allows us to establish the correspondence between the applied magnetic field directions and the crystallographic axes in the subsequent analysis.

The atomically resolved image acquired on a defect-free area below T_c reveals chains of Te1 atoms along *a*-axis (Fig. 1*C*), and the corresponding fast Fourier transform (FFT) is shown in Fig. 1*D*. Beyond the previously reported q_i CDW orders (marked by squares), a new set of $h_{1,2}$ and p_3 peaks emerge at zero field (marked by blue/red triangles and a green circle). By performing spectroscopic imaging via *dI/dV* maps, we obtain the real-space distribution of the local density of states (LDOS), whose FFTs capture the energy-dependent spectral weight in momentum space, enabling a distinction between quasiparticle interference and CDW signatures. Fig. 1 *E–G* present the FFTs of *dI/dV* maps at the indicated energies, including one within and two well above the superconducting gap, where the $h_{1,2}$ and p_3 peaks are clearly visible (see *SI Appendix*, Figs. S2 and S3 for the full dataset). We investigate the energy dependence of the $h_{1,2}$ and p_3 peaks, by performing line cuts along the three momentum directions (Fig. 1*E*). These peaks remain nondispersive across the measured energy range extending to energies far above the superconducting gap (Fig. 1 *I–K*), manifesting their origin as CDW orders rather than their previous identification as QPI features (26, 27). The wavevectors of $h_{1,2}$ and p_3 orders are $\{\mathbf{h}_1, \mathbf{h}_2, \mathbf{p}_3\} = \{(-0.26, -0.14), (0.26, -0.14), (0, -0.28)\}|q_{Te}|$, where $|q_{Te}|$ denotes the Bragg wavevector of the Te lattice. All three vectors have comparable magnitudes and together form a hexagonal lattice–like periodic modulation in real space (*SI Appendix*, Fig. S4). Interestingly, the line profile extracted along line 3 in Fig. 1*E* shows that the magnitude of the p_3 peak is approximately half that of q_3 (Fig. 1*H*). The significance of this relationship will be discussed later in the paper. It is also worth noting that the interference of defects most likely hindered the observation of the $h_{1,2}$ and p_3 CDW orders in previous studies (22–24). This is because in reciprocal space, defect-induced electronic states can generate intense spectral weight near zero momentum, with momentum components similar to those of the $h_{1,2}$ and p_3 wavevectors, thereby smearing or obscuring these intrinsic CDW features (*SI Appendix*, Fig. S5).

A systematic, temperature-dependent study was carried out to determine the onset temperatures of the newly identified $h_{1,2}$ and p_3 orders. Since the CDW transition in UTe_2 currently lacks a clear bulk signature (28–30) and appears to be confined to the surface, STM enables a direct characterization of the CDW evolution with temperature in a momentum-resolved manner. Fig. 2 *A–G* present a series of normalized FFTs of STM topographies acquired at the indicated temperatures. Across the superconducting transition at $T_c = 2.1$ K, the p_3 CDW peak exhibits the most significant change among all CDW components, being strongly suppressed above the transition temperature. This is clearly reflected in Fig. 2 *H* and *I*, which show the $h_{1,2}$, p_3, and q_i peak intensities extracted from the FFTs. The q_i CDW intensities decrease with temperature and are markedly reduced at 4.8 K, consistent with our previous report (23). In contrast, the p_3 CDW intensity decreases progressively with increasing temperature, becoming close to the background above T_c.

[*]In the previous definition (23), the PDWs had wavevector q_i and the q_i CDWs were taken to arise from the combination of PDWs and uniform superconductivity.

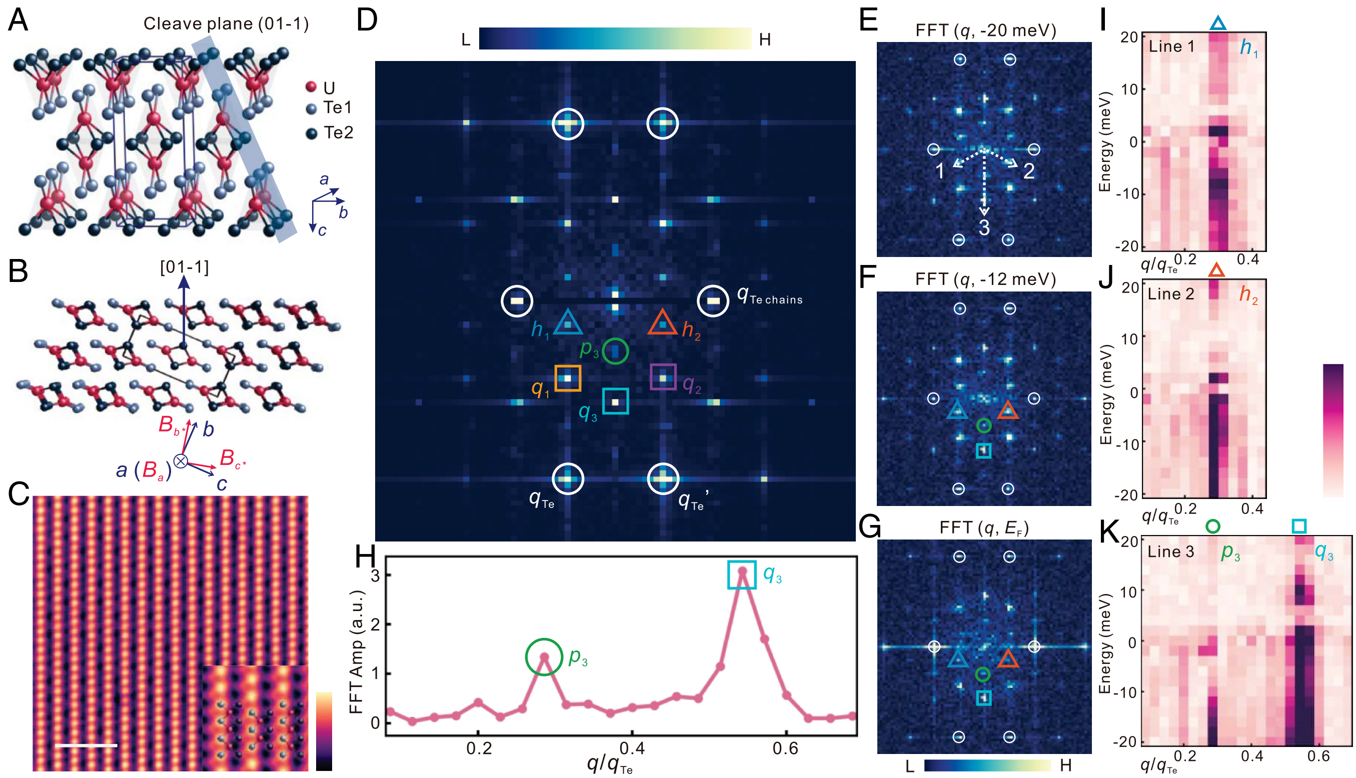

Fig. 1. Crystal structure and two distinct sets of CDW orders of UTe_2. (*A*) Structural framework of UTe_2. The orthorhombic unit cell and the (01-1) cleavage plane are delineated by a rectangular box and a blue plane, respectively. Each U (red) atom is coordinated by two inequivalent Te sites, denoted Te1 (light blue) and Te2 (dark blue). (*B*) Side-view schematic of (01-1) plane. Relations between externally applied magnetic fields (B_a, B_{b*}, and B_{c*}) and the crystallographic axes are illustrated. The B_a direction is parallel to the *a*-axis, while the B_{b*} and B_{c*} fields are counterclockwise tilted by approximately 12° relative to the crystallographic *b* and *c* axes, respectively. (*C*) Atomic-resolution image acquired on defect free region at 300 mK (V = 20 mV, I = 100 pA). (Scale bar, 3 nm.) The *Inset* shows the configuration of Te1 (light blue) and Te2 (dark blue) atoms with lattice schematic overlaid on *Top*. (*D*) Fourier transform of the topography shown in *C*. The Bragg peaks arising from Te1 atoms are marked by white circles ($\pm q_{Te}$, $\pm q_{Te}'$, $\pm q_{Te\ chains}$; only one side is labeled for clarity). Squares colored yellow (q_1), purple (q_2), and cyan (q_3) denote the experimentally confirmed set of CDW peaks. Additionally, a newly observed set of CDW orders under zero field is indicated by blue (h_1) and red (h_2) triangles, as well as a green circle (p_3). (*E*–*G*) FFTs of LDOS maps shown in *SI Appendix*, Fig. S2 at 300 mK for the indicated energies. The new set of CDW modulations (h_1, h_2 and p_3), marked by blue/red triangles and a green circle, is clearly visible at all energies. The Bragg peaks are marked by white circles (V = 20 mV, I = 150 pA). (*H*) Line cut extracted along line 3 indicated in *E*. The magnitude of p_3 is approximately half that of q_3. (*I*–*K*) The intensity maps plotted by line cuts extracted from FFTs at various energies along the dashed lines in *E*. The magnitude of the h_1, h_2 and p_3 wavevectors remains constant with energy, consistent with their identification as CDW signals. All three CDW wavevectors exhibit similar magnitudes, approximately 0.28 q_{Te}.

This suggests a relationship between p_3 and the uniform superconducting order. Equally importantly, the p_3 and q_3 peaks emerge at different onset temperatures, which strongly indicates that they are not harmonically related wavevectors as was previously hypothesized (25), and instead points to a different mechanism governing the interplay between the p_i and q_i peaks. We will investigate this possibility in the remainder of the paper.

Before proceeding with further discussions on the possible origins of the p_3 peak, we look for signatures of p_1 and p_2 peaks which were previously observed in magnetic fields at 30mK temperatures (25). To this end, we employ a vector magnet that enables independent tuning of all three magnetic field components, with their orientations relative to the crystallographic axes of UTe_2 defined throughout this work as illustrated in Fig. 1*B*. Specifically, the laboratory axis B_y is aligned with crystallographic *a*-axis, while B_x and B_z are tilted counterclockwise by approximately 12° from the *c*- and *b*-axes, respectively (see *SI Appendix*, Fig. S6 for details). For simplicity, we label the magnetic field directions B_x, B_y, B_z, as B_{c^*}, B_a, B_{b^*} to reflect their approximate alignment with the crystallographic *c*-, *a*-, and *b*-axes, respectively. This field-axis convention is based on the assumption that the sample cleaved along the (01-1) plane. We note that density functional theory calculations indicate that Te2 p orbitals dominate the density of states at the Fermi level (31), suggesting that the visually dominant chains in the STM topography may correspond to Te2 atoms, implying a cleavage along the (011) plane (*SI Appendix*, Fig. S6). This would modify the relative orientation between the laboratory and crystallographic axes, but B_{b^*} and B_{c^*} remain primarily aligned with the *b*- and *c*-axes, leaving our conclusions unchanged.

Fig. 3 *A*–*D* present the FFTs of topographic images acquired at 300 mK under the indicated magnetic field directions and magnitudes. Compared with the zero-field result (Fig. 3*A*), a consistent feature across field configurations in Fig. 3 *B*–*D* is the emergence of a field-induced p_2 peak, whose wavevector magnitude is half that of q_2. Energy-dependent measurements further confirm that the p_2 peak, originates from a CDW order (see *SI Appendix*, Fig. S7 for details). The CDW peaks observed at 0 T (h_1, h_2, p_3, q_1, q_2, q_3) and those appearing under finite magnetic fields (p_1 and p_2) are summarized in Fig. 3*E*, which illustrates their distribution in momentum space. The analogous wavevector relations, $p_{2,3} = 1/2 q_{2,3}$, suggest that the p_2 and p_3 CDWs share a common origin. To explore this connection, we perform systematic vector field- and temperature-dependent measurements, focusing on the evolution of the p_2 order.

We first construct the field-temperature phase diagram with magnetic field along b^* (B_{b^*}) by plotting the intensity of the p_2 peak. As seen in Fig. 3*F* (see full dataset in *SI Appendix*, Fig. S8), at 300 mK, the p_2 peak appears at an onset field H_{onset} of ~5 T and persists up to 8 T. As the temperature increases to 1.6 K, the field range sustaining p_2 shrinks to approximately 5 to 6 T, and its intensity becomes

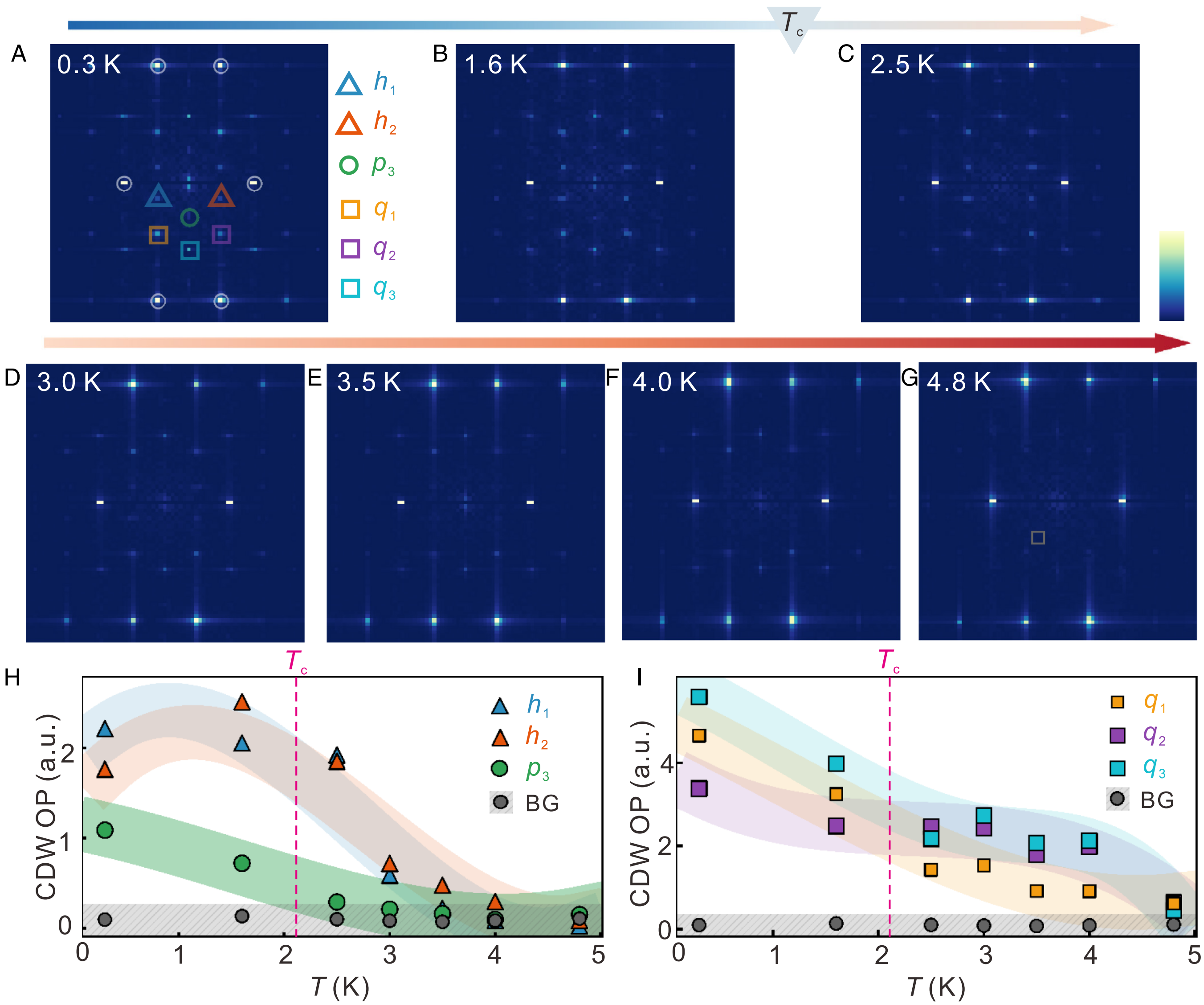

Fig. 2. Temperature-dependent suppression of the $h_{1,2}$, p_3, and q_i CDW orders. (*A*–*G*) FFTs acquired on the same area at the indicated temperatures, maintaining identical set points (V = 20 mV, I = 100 pA). The intensities of FFT images are normalized by q_{Te} and q_{Te}'. The amplitude of the p_3 peak (green circle) rapidly diminishes upon crossing the superconducting transition temperature (T_c = 2.1 K) of UTe_2. Peaks h_1 (blue triangle) and h_2 (red triangle) vanish at approximately 3.5 K. The intensity of the previously identified q_i CDW continuously weakens with increasing temperature, becoming significantly attenuated by 4.8 K. The Bragg peaks are marked by white circles in *A*. (*H*) Temperature dependence of the intensities of $h_{1,2}$, p_3 peaks. (*I*) Same as *H*, but for the q_i peak intensities. Extracted peak intensities are normalized relative to q_{Te} and q_{Te}'. Scatter points are color-coded according to their corresponding CDW labels, and shaded areas of matching colors serve as visual guides to indicate overall intensity trends. The background intensity (BG), extracted from FFT regions free of CDW peaks (gray square in *G*), is shown as gray solid circles with hatched shading and remains nearly constant with temperature.

weaker. The field at which the intensity is suppressed below the background (H_{sup}) decreases with increasing temperature, and the p_2 feature disappears entirely when the temperature exceeds T_c (i.e., 2.5 K). Similar measurements under B_a and B_{c^*} show a comparable trend (Fig. 3 *G* and *H*). For a given B_a magnetic field, the p_2 peak progressively weakens with increasing temperature and disappears above T_c (Fig. 3*G*, see full dataset in *SI Appendix*, Fig. S9). At 300 mK, the p_2 peak strengthens with increasing B_{c^*} up to 2 T (Fig. 3*H*, see full dataset in *SI Appendix*, Fig. S10). These results indicate that the field-induced p_2 modulation exhibits a similar temperature dependence to the zero-field p_3 peak and is connected to uniform superconductivity. H_{onset} for p_2 is substantially larger for fields along b^* than along a and c^* (~0.5 T at 300 mK), indicating a higher threshold for the emergence of p_2 near the b axis, consistent with the b-axis being the magnetic hard axis of UTe_2 and hosting the largest H_{c2}. Additionally, the p_1 CDW peak, which is the mirror counterpart of p_2, emerges under B_{b^*} in another field of view (*SI Appendix*, Fig. S11). Finally, we note that in contrast to the p_3 and p_2 CDWs, the q_i CDWs persists under the same field conditions at temperatures below 2.5 K.

So far, we have established i) that all $h_{1,2}$ and $p_{1,2,3}$ orders are visible at energies far above the superconducting gap and do not disperse which suggests that they are not related to nodal in-gap QPI; ii) p_3 is visible in zero field while $p_{1,2}$ emerge at a finite field; and iii) the differing magnetic field behavior and onset temperatures of the q_i and p_i orders indicate that despite their commensurate relationship i.e., $p_i = 1/2q_i$, the q_i order is not a simple harmonic of the p_i order.

The final piece of the puzzle is to ascertain whether the original q_i CDW order exhibits field sensitivity at elevated temperatures (>T_c). To do this we performed vector-field measurements at 4.2 K. As expected from the temperature dependence shown in Fig. 2, the FFT of the LDOS map at 4.2 K and zero field (Fig. 4*A*) reveal only the energy-independent q_i peaks (*SI Appendix*, Fig. S12), with a schematic of these CDW wavevectors shown in Fig. 4*B*. Upon applying magnetic fields along or near the crystallographic axes

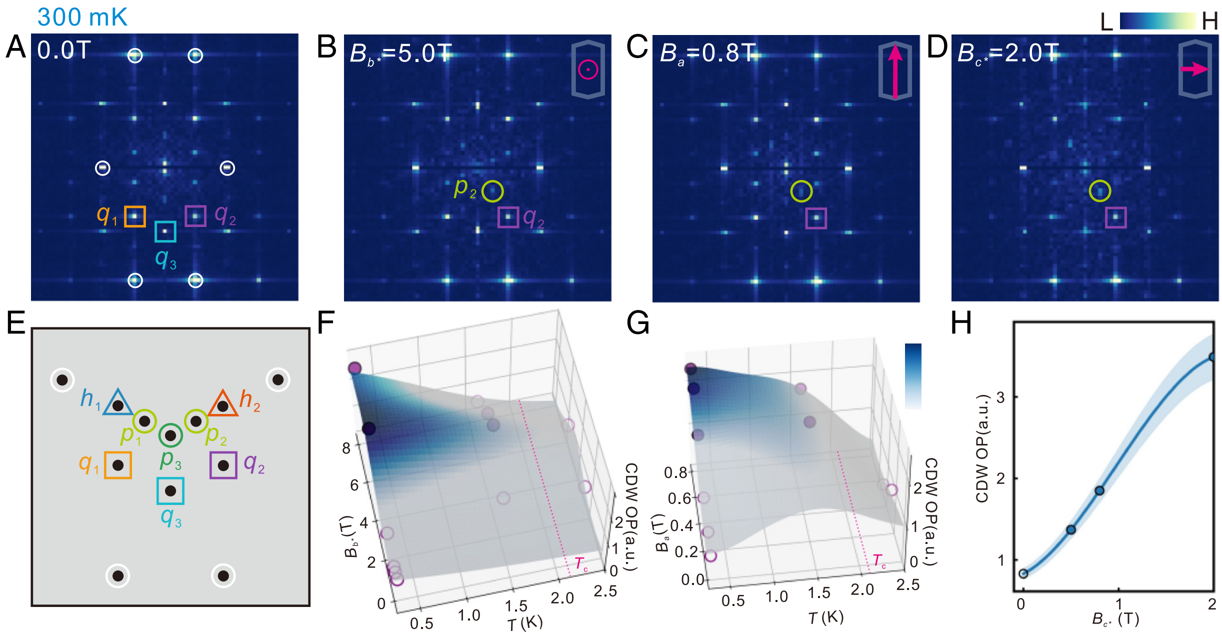

Fig. 3. Magnetic field and temperature evolution of the field-induced CDW peak p_2. (*A*–*D*) FFTs obtained on the same area at the indicated magnetic fields under consistent experimental conditions (T = 300 mK, V = 20 mV, I = 100 pA). The orientations of applied fields (B_{b^*}, B_a, and B_{c^*}) relative to crystal axes are illustrated in Fig. 1*B*. An additional CDW peak, p_2 (light green circle), emerges under various field configurations and exhibits a wavevector magnitude equal to half of q_2 (purple square). The Bragg peaks are marked by white circles in *A*. (*E*) Schematic summary of CDW peaks observed at 0 T (h_1, h_2, p_3, q_1, q_2, q_3) and under finite magnetic fields (p_1 and p_2) at 300 mK. White circles indicate Bragg points. (*F*) Three-dimensional plot of the p_2 CDW peak intensity as functions of temperature and magnetic field along the B_{b^*} direction. Peak p_2 appears at 5 T and persists at least to 8 T at 300 mK, remains detectable at narrower field range at 1.6 K, and is absent at 2.5 K. (*G*) Same as *F*, but with magnetic field applied along the B_a direction. The peak arises around 0.5 T at 300 mK, intensifies with increasing field, persists at 1.6 K under corresponding magnetic fields, and vanishes at 2.5 K. (*H*) Dependence of p_2 CDW peak intensity on magnetic field applied along the B_{c^*} direction at 300 mK. The peak emerges at approximately 0.5 T and is enhanced by further increasing the field. Solid circles and open circles in *F*–*H* indicate the presence and absence of the p_2 peak at the corresponding magnetic fields and temperatures, respectively. All intensities presented in *F*–*H* are normalized with respect to q_{Te} and q_{Te}'. Complete FFT datasets are provided in *SI Appendix*, Figs. S8–S10.

(B_{b^*} = 4.0 T, B_a = 0.4 T, and B_{c^*} = 1.5 T), the q_i peaks exhibit a reduction in intensity but remain discernible (Fig. 4 *C*, *E*, and *G*). With further increase in field strength (B_{b^*} = 8.0 T, B_a = 0.8 T, and B_{c^*} = 3.0 T), the q_i peaks are nearly or completely suppressed along all directions (Fig. 4 *D*, *F*, and *H*). All datasets were acquired over the same spatial region using identical bias setpoints and energies, ensuring that the observed changes are exclusively field-induced. Compared to the results at lower temperatures where the q_i modulation persists under the same field magnitudes (*SI Appendix*, Figs. S8–S10), we conclude that H_{sup} of the q_i order decreases dramatically with increasing temperature. Specifically, at 4.2 K, H_{sup} falls within the ranges $4.0 < H_{sup}^{b^*} < 8.0$ T, $0.4 < H_{sup}^{a} < 0.8$ T and $1.5 < H_{sup}^{c^*} < 3.0$ T along the b^*-, a-, and c^*-axis directions, respectively.

By extracting the normalized intensity of each q_i peak from the FFTs, we can track its evolution as a function of magnetic field strength for each crystallographic direction (Fig. 4 *I*–*K*). Scaling the applied field B_n (n = a, b^*, c^*) by the corresponding upper critical field H_{c2} reveals the anisotropic relation $H_{sup}^{b^*} > H_{sup}^{c^*} > H_{sup}^{a}$ for all q_i peaks, in agreement with the established hierarchy of $H_{c2}^{b^*} > H_{c2}^{c^*} > H_{c2}^{a}$. Since superconductivity is fully suppressed at 4.2 K, this correlation between the anisotropy of H_{sup} and H_{c2} provides compelling evidence that the q_i CDW order is intertwined with a PDW component.

Finally, with comprehensive temperature- and field-dependent data in hand, we are now positioned to address the origins of the $p_{1,2,3}$ (p_i) peaks and their relation to the previously identified $q_{1,2,3}$ (q_i) CDW peaks, as well as the emergence of the h_1 and h_2 peaks. In our previous work, the q_i CDW peaks were identified as composite orders which formed from the combination of wavevector q_i PDWs and uniform superconductivity (23). With the new information in this study, we can provide a more refined explanation for the results.

As we shall now show, the magnetic field sensitivity of the $q_{1,2,3}$ CDW peaks above the bulk T_c and the formation of the p_3 CDW at the bulk T_c, can both be explained by the existence of a PDW that forms with a higher critical temperature than the bulk T_c, and coexists with uniform superconductivity below T_c. Let us consider the following minimal Landau free energy for the CDW and PDW orders:

$$\begin{aligned}\mathcal{F} = &\sum_i \alpha_i\left(T - T_{PDW}\right)|\Psi_{p_i}|^2 + \lambda_i|\Psi_{p_i}|^4 + \alpha_0\left(T - T_c\right)|\Psi_0|^2 + \lambda_0|\Psi_0|^4 \\ &+ \sum_i r_{1,i}\left|\rho_{p_i}\right|^2 + \sum_i r_{2,i}\left|\rho_{2p_i}\right|^2 + r_4\left[\left|\rho_{2p_3-2p_2}\right|^2 + \left|\rho_{2p_3-2p_1}\right|^2\right] \\ &+ \sum_i g_{1,i}\,\rho_{p_i}\left[\Psi_0\Psi_{p_i}^* + \Psi_0^*\Psi_{-p_i}\right] + \sum_i g_{2,i}\,\rho_{2p_i}\Psi_{-p_i}\Psi_{p_i}^* \\ &+ \sum_i \gamma_{1,i}\rho_{p_i}\rho_{p_i}\rho_{2p_i}^* + \gamma_2\left[\rho_{2p_3}\,\rho_{-2p_2}\,\rho_{2p_3-2p_2}^* + \rho_{2p_3}\,\rho_{-2p_1}\,\rho_{2p_3-2p_1}^*\right] + c.c\end{aligned} \quad [1]$$

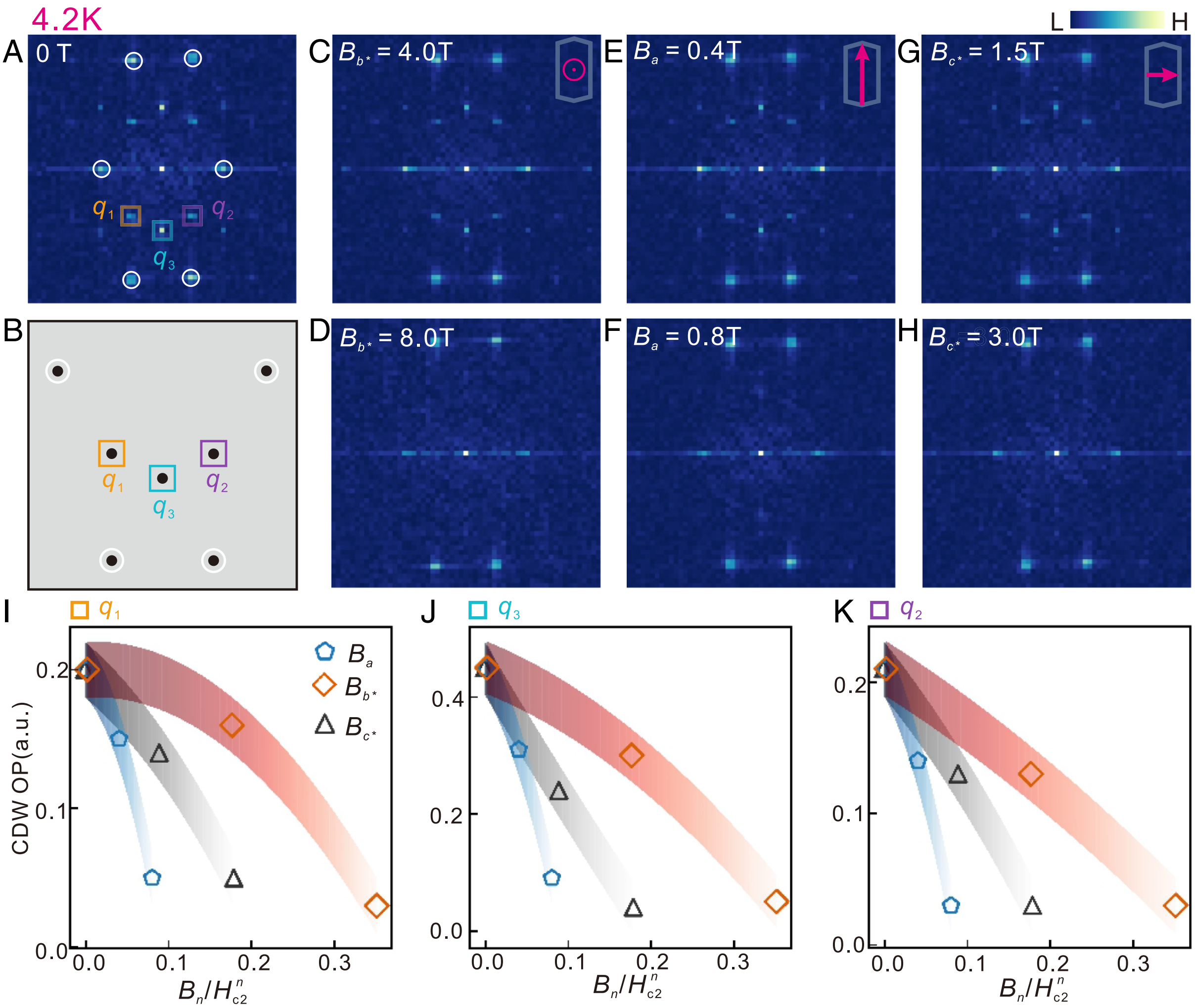

Fig. 4. Magnetic field dependence of the q_i CDW orders above T_c (4.2 K). (*A*) FFT of the LDOS map acquired at −20 mV and 4.2 K under zero magnetic field, where only the q_i CDW is visible. The Bragg peaks are marked by white circles (V = 20 mV, I = 150 pA). (*B*) Schematic of the q_i CDW peaks observed at 4.2 K. White circles indicate Bragg peaks. (*C*–*H*) FFTs of LDOS maps acquired at −20 mV and 4.2 K under the indicated magnetic fields. All measurements were performed in the same area as in *A*, using identical set-point conditions (V = 20 mV, I = 150 pA). The q_i CDW peaks are completely suppressed in *D* (B_{b^*} = 8.0 T) and *H* (B_{c^*} = 3.0 T). Peaks q_1 and q_2 are entirely suppressed, whereas q_3 remains only barely visible in *F* (B_a = 0.8 T). The intensities of FFT images are normalized by q_{Te} and q_{Te}'. (*I*–*K*) Intensity variations of the three CDW peaks q_1 (yellow square), q_3 (cyan square), and q_2 (purple square) as functions of vector magnetic fields B_n (n = a, b^*, c^*), respectively. The field values along each direction are scaled by the corresponding H^n_{c2} (n = a, b^*, c^*) of UTe_2. All extracted intensities of the q_i peaks are normalized with respect to q_{Te} and q_{Te}'. The magnetic fields required to fully suppress the q_i CDW peaks differ along the three field directions following the order $H^{b^*}_{sup} > H^{c^*}_{sup} > H^{a}_{sup}$, which aligns with the corresponding trend of H_{c2}, namely, $H^{b^*}_{c2} > H^{c^*}_{c2} > H^{a}_{c2}$.

Here, Ψ_{p_i} is the PDW order parameter at wavevector p_i, and similarly, Ψ_0 is the uniform superconducting order parameter. While these order parameters nominally describe spin triplet superconductivity, due to the spin–orbit coupling, they are formally scalars that transform as irreducible representations of the crystal symmetries of system (32). T_{PDW} is the transition temperature of the PDW, which we take to be the same as the temperature where the q_i CDW forms (approximately 5 K). T_c is the critical temperature for the bulk uniform superconductivity (approximately 2.1 K). Note that we have not included all symmetry allowed terms in the free energy. In particular, in Eq. **1** we have not included possible biquadratic terms, which will encode competitions or cooperation between different phase orderings. However, these additional terms are not necessary for discussing the PDW induced CDWs. Also, in Eq. **1** we have not included the effects of quenched random disorder (i.e., impurities) which couples strongly to any nonuniform order and, ultimately, destroys long range PDW and CDW orders over length scales larger than the field of view of our STM experiments.

Table 1 tabulates the observed CDW vectors and their connections to the PDW and uniform superconductivity (see Fig. 3*E* for their momentum-space distribution). In the following, we discuss the microscopic origin of these CDWs at different temperature regimes. When $T > T_{PDW}$, both PDW and superconducting orders are disordered $(\langle\Psi_{p_i}\rangle = \langle\Psi_0\rangle = 0)$, thus no CDW signal is observed. In the intermediate regime $T_{PDW} > T > T_c$, the PDWs become ordered $(\langle\Psi_{p_i}\rangle \neq 0)$ while the uniform superconductivity remains disordered $(\langle\Psi_0\rangle = 0)$. The PDWs give rise to charge modulations at wavevector $2p_i$, $\rho_{q_i} \propto \Psi_{p_i}\Psi^*_{-p_i}$, due to the trilinear coupling between the different order parameters. These modulations correspond to the experimentally observed q_i CDW peaks. The magnetic-field sensitivity of the q_i peaks in this regime is governed by the same mechanism proposed in our previous work (23).

At temperatures below T_c, both the PDW and uniform superconductivity orders are established $(\langle\Psi_{p_i}\rangle \neq 0, \langle\Psi_0\rangle \neq 0)$. The combination of PDWs and uniform superconductivity can give rise to wavevectors p_i CDWs, $\rho_{p_i} \propto \Psi_{p_i}\Psi^*_0 + \Psi^*_{-p_i}\Psi_0$. Among

Table 1. Summary of the observed CDW vectors and their relationship to the PDW and uniform superconductivity

CDW vectors	Category	Physical origin	Representative expressions
p_i (i = 1,2,3)	Fundamental (low T)	Composite of p_i PDWs and uniform superconductivity	$\rho_{p_i} \propto \Psi_{p_i}\Psi_0^* + \Psi_{-p_i}^*\Psi_0$
q_i (i = 1,2,3)	Fundamental (high T)	Composite of p_i PDWs	$\rho_{q_i} \propto \Psi_{p_i}\Psi_{-p_i}^*$
$h_{1,2}$	Harmonic-derived	Harmonic of q_i CDWs	$h_1 = q_3 - q_2$ $h_2 = q_3 - q_1$

these CDWs, only p_3 is observed at zero field, while p_1 and p_2 emerge under an applied magnetic field and are theoretically expected to arise from the same superconductivity-coupled mechanism. Within this theory, this implies that the relative phase between Ψ_0 and $\Psi^*_{\pm p_{1,2}}$ is $\pi/2$, while the relative phase shift between Ψ_0 and $\Psi^*_{\pm p_3}$ is not $\pi/2$. It is worth noting that if the phase shift between Ψ_0 and $\Psi^*_{\pm p_{1,2}}$ is $\pi/2$, there will be composite SDW order with wavevector $p_{1,2}$, $S_{p_i} \propto i\Psi_{p_i}\Psi_0^* - i\Psi^*_{-p_i}\Psi_0$. The observation of the p_1 and p_2 CDWs in finite magnetic field is explained by the fact that an external magnetic field breaks time reversal symmetry and mixes S_{p_i} into ρ_{p_i}, leading to a nonzero expectation value for ρ_{p_i}. As we shall discuss in the next section, the PDW would have to be localized at the surface of the system in a consistent theory, and the SDWs would be localized at the surface as well. Detecting the SDWs would require a surface-sensitive probe, such as spin-polarized STM.

From this analysis, we find that all the q_i and p_i CDWs orders can be consistently understood as arising from PDWs and uniform superconductivity. This scenario does, however, rest on the strong assumption that the PDWs form above the bulk T_c. Given that there is no bulk evidence of a PDW above T_c, such a state would have to be localized to the surface of the sample. In principle, a surface PDW can occur above the bulk T_c, as the energetics of the surface may be very different than those of the bulk. A microscopic theory would be needed to determine if a surface PDW can, in fact, arise in this way. An alternative possibility is that the p_i and q_i peaks originate from spin-related density wave orders. This interpretation appears less likely for the several reasons. Our STM measurements, performed with a conventional non-spin-polarized tip, are not directly sensitive to a pure SDW signal. Although a CDW could in principle be associated with an SDW at half the wavevector, such an SDW/CDW explanation for the peaks would not be consistent with the generation of magnetic-field induced dislocations that ultimately destroy the CDW state (23, 24). This scenario is further inconsistent with the fact that, by symmetry, a uniform magnetic field does not couple to an SDW state, except very close to a transition to a spin-polarized state, whereas our results reveal a pronounced field response even above the bulk T_c. Moreover, this picture fails to explain the distinct temperature evolution of the p_i and q_i peaks revealed by our data. Taken together, these observations are therefore difficult to reconcile with a simple spin-related density wave scenario. It has also been proposed that the CDW itself acts as the primary instability, leading to a multicomponent PDW upon coupling to bulk superconductivity (33). However, the field sensitivity of the q_i peaks observed above the bulk T_c is likewise incompatible with a preexisting CDW, which should be insensitive to an applied magnetic field in the absence of superconductivity.

Based on the refined PDW framework, we are now able to elucidate the origin of the h_1 and h_2 modulations. In fact, the h_1 and h_2 modulations can be interpreted as harmonic-derived, higher-order composite CDWs. Since $h_1 = 2p_3 - 2p_2 = q_3 - q_2$, the equation of motion for $\rho_{2p_3-2p_2}$ show that the h_1 CDW can arise as a composite of the q_3 and $-q_2$ CDWs, or equivalently, as a fourth-order composite of PDW components. Similarly, the h_2 CDW corresponds to $\rho_{2p_3-2p_1}$ and can arise as a composite of the q_3 and $-q_1$ CDWs. This explanation also accounts for the similarities between the magnetic field responses of the $h_{1,2}$ CDWs (*SI Appendix*, Figs. S8 and S9) and those of the q_i CDWs (23).

Our results reveal a hierarchy of intertwined electronic orders in UTe_2. The vector-field and temperature-dependent measurements of the high-temperature $q_{1,2,3}$ and low-temperature $h_{1,2}$, $p_{1,2,3}$ CDW modulations point toward a PDW-based explanation, where wavevector p_i PDWs form above T_c, leading to the $q_{1,2,3}$ and $h_{1,2}$ charge modulations, while the $p_{1,2,3}$ peaks emerge through coupling to uniform superconductivity below T_c. This is captured by a Landau free energy which couples the PDW, uniform superconductivity and CDW order parameters to one another. Our findings offer crucial insights into the nature of PDW states and their role in generating intertwined orders in strongly correlated systems.

Methods

Single crystals of UTe_2 grown by a molten flux method were used. The growth and characterization are mentioned in detail elsewhere (19). The STM measurements were performed in a Unisoku STM operating under ultrahigh vacuum and a vector magnetic field (H_x:4T, H_y:1T, H_z:9T). The UTe_2 single crystals were cleaved in situ at about 90 K and then transferred immediately into STM head. All the measurements were carried out at 300 mK (unless otherwise specified) using tungsten tips treated with heating in situ. *dI/dV* signals were acquired by a standard lock-in amplifier with modulation of 500 μV at 991 Hz, unless otherwise noted.

Note. After the submission of our manuscript, we became aware of several related studies on UTe_2 uploaded to arXiv at a similar time (34–36). They also reported similar CDW orders, but attributed their origin to distinct mechanisms, including Kondo-related electronic orders (34, 35) and a surface parent spin order (36).

Data, Materials, and Software Availability. All study data have been deposited in Zenodo (37).

ACKNOWLEDGMENTS. STM studies at the University of Illinois, Urbana-Champaign, were supported by the US Department of Energy, Office of Science, Office of Basic Energy Sciences, Materials Sciences and Engineering Division under award number DE-SC0022101. V.M. acknowledges partial support from the Gordon and Betty Moore Foundation's EPiQS Initiative through grant GBMF4860 and the Quantum Materials Program at CIFAR where she is a Fellow. Theoretical work was supported in part by NSF grant DMR 2225920 (E.F.). A.G.E. acknowledges support from the Henry Royce Institute for Advanced Materials through the Equipment Access Scheme enabling access to the Advanced Materials Characterization Suite at Cambridge, grant numbers EP/P024947/1, EP/M000524/1, and EP/R00661X/1, and from Sidney Sussex College (University of Cambridge). A.C. and M.V. acknowledge support by the Czech Science Foundation GAČR under the Junior Star Grant No. 26-21795M (STiUS). Crystals were grown and characterized in MGML (mgml.eu), which is supported within the program of Czech Research Infrastructures (project No. LM2023065). Research at the University of Maryland was supported by the Gordon and Betty Moore Foundation's EPiQS Initiative Grant No. GBMF9071, the NIST Center for Neutron Research, and the Maryland Quantum Materials Center. This work was initiated in part at Aspen Center for Physics, which is supported by National Science Foundation grant PHY-2210452.

Author affiliations: [a]Department of Physics and Materials Research Laboratory, Grainger College of Engineering, University of Illinois at Urbana-Champaign, Urbana, IL 61801; [b]Department of Physics, Stanford University, Stanford, CA 94305; [c]Department of Physics, Cavendish Laboratory, University of Cambridge, Cambridge CB3 0HE, United Kingdom; [d]Maryland Quantum Materials Center, Department of Physics, University of Maryland, College Park, MD 20742; [e]Canadian Institute for Advanced Research, Toronto, ON M5G 1Z8, Canada; [f]Department of Condensed Matter Physics, Faculty of Mathematics and Physics, Charles University, Prague 2 121 16, Czech Republic; and [g]Institute for Condensed Matter Theory, Grainger College of Engineering, University of Illinois at Urbana-Champaign, Urbana, IL 61801

1. E. Fradkin, S. A. Kivelson, J. M. Tranquada, Theory of intertwined orders in high temperature superconductors. *Rev. Mod. Phys.* **87**, 457 (2015).
2. E. Fradkin, Intertwined orders and the physics of high temperature superconductors. *Particles* **8**, 70 (2025).
3. D. F. Agterberg *et al.*, The physics of pair-density waves: Cuprate superconductors and beyond. *Annu. Rev. Condens. Matter Phys.* **11**, 231 (2020).
4. Z. Dai, Y.-H. Zhang, T. Senthil, P. A. Lee, Pair-density waves, charge-density waves, and vortices in high-T_c cuprates. *Phys. Rev. B* **97**, 174511 (2018).
5. M. H. Hamidian *et al.*, Detection of a Cooper-pair density wave in $Bi_2Sr_2CaCu_2O_{8+x}$. *Nature* **532**, 343 (2016).
6. S. D. Edkins *et al.*, Magnetic field–induced pair density wave state in the cuprate vortex halo. *Science* **364**, 976 (2019).
7. J.-S. Lee *et al.*, Pair-density wave signature observed by x-ray scattering in La-based high-T_c cuprates. arXiv [Preprint] (2023). https://doi.org/10.48550/arXiv.2310.19907 (Accessed 30 October 2023).
8. X. Liu, Y. X. Chong, R. Sharma, J. C. S. Davis, Discovery of a Cooper-pair density wave state in a transition-metal dichalcogenide. *Science* **372**, 1447 (2021).
9. L. Cao *et al.*, Directly visualizing nematic superconductivity driven by the pair density wave in $NbSe_2$. *Nat. Commun.* **15**, 7234 (2024).
10. F.-J. Cheng *et al.*, Imaging sublattice Cooper-pair density waves in monolayer 1T′-$MoTe_2$. *Phys. Rev. Lett.* **135**, 166201 (2025).
11. H. Chen *et al.*, Roton pair density wave and unconventional strong-coupling superconductivity in a topological kagome metal. *Nature* **599**, 222 (2021).
12. X. Han *et al.*, Atomic manipulation of the emergent quasi-2D superconductivity and pair density wave in a kagome metal. *Nat. Nanotechnol.* **20**, 1017 (2025).
13. H. Zhao *et al.*, Smectic pair-density-wave order in $EuRbFe_4As_4$. *Nature* **618**, 940 (2023).
14. Y. Liu *et al.*, Pair density wave state in a monolayer high-T_c iron-based superconductor. *Nature* **618**, 934 (2023).
15. S. Ran *et al.*, Nearly ferromagnetic spin-triplet superconductivity. *Science* **365**, 684 (2019).
16. S. Ran *et al.*, Extreme magnetic field-boosted superconductivity. *Nat. Phys.* **15**, 1250 (2019).
17. L. Jiao *et al.*, Chiral superconductivity in heavy-fermion metal UTe_2. *Nature* **579**, 523 (2020).
18. D. Aoki, Molten salt flux liquid transport method for ultra clean single crystals UTe_2. *J. Phys. Soc. Jpn.* **93**, 043703 (2024).
19. A. G. Eaton *et al.*, Quasi-2D Fermi surface in the anomalous superconductor UTe_2. *Nat. Commun.* **15**, 223 (2024).
20. I. M. Hayes *et al.*, Robust nodal behavior in the thermal conductivity of superconducting UTe_2. *Phys. Rev. X* **15**, 021029 (2025).
21. Z. Wu *et al.*, Enhanced triplet superconductivity in next-generation ultraclean UTe_2. *Proc. Natl. Acad. Sci. U.S.A.* **121**, e2403067121 (2024).
22. Q. Gu *et al.*, Detection of a pair density wave state in UTe_2. *Nature* **618**, 921 (2023).
23. A. Aishwarya *et al.*, Magnetic-field-sensitive charge density waves in the superconductor UTe_2. *Nature* **618**, 928 (2023).
24. A. Aishwarya *et al.*, Melting of the charge density wave by generation of pairs of topological defects in UTe_2. *Nat. Phys.* **20**, 964 (2024).
25. P. García Talavera *et al.*, Surface charge density wave in UTe_2. arXiv [Preprint] (2025). https://doi.org/10.48550/arXiv.2504.12505 (Accessed 16 April 2025).
26. S. Wang *et al.*, Odd-parity quasiparticle interference in the superconductive surface state of UTe_2. *Nat. Phys.* **21**, 1555 (2025).
27. Q. Gu *et al.*, Pair wave function symmetry in UTe_2 from zero-energy surface state visualization. *Science* **388**, 938 (2025).
28. C. S. Kengle *et al.*, Absence of a bulk signature of a charge density wave in hard x-ray measurements of UTe_2. *Phys. Rev. B* **110**, 145101 (2024).
29. C. S. Kengle *et al.*, Absence of bulk charge density wave order in the normal state of UTe_2. *Nat. Commun.* **15**, 9713 (2024).
30. F. Theuss *et al.*, Absence of a bulk thermodynamic phase transition to a density wave phase in UTe_2. *Phys. Rev. B* **110**, 144507 (2024).
31. F. Theuss *et al.*, Single-component superconductivity in UTe_2 at ambient pressure. *Nat. Phys.* **20**, 1124 (2024).
32. D. F. Agterberg, M. Sigrist, H. Tsunetsugu, Order parameter and vortices in the superconducting Q phase of $CeCoIn_5$. *Phys. Rev. Lett.* **102**, 207004 (2009).
33. A. L. Szabó, A. Ramires, Intertwining bulk and surface: The case of UTe_2. *Phys. Rev. Res.* **8**, L012038 (2026).
34. X. Yu *et al.*, Observation of Kondo hybridization wave in UTe_2. arXiv [Preprint] (2026). https://doi.org/10.48550/arXiv.2603.10552 (Accessed 11 March 2026).
35. N. Sharma *et al.*, Directional manipulation of a staggered charge density wave and Kondo resonance in UTe_2. arXiv [Preprint] (2026). https://doi.org/10.48550/arXiv.2603.12097 (Accessed 12 March 2026).
36. Y. Li *et al.*, Magnetic-field-tunable commensurate multi-q charge orders on UTe_2 (011) surface. arXiv [Preprint] (2026). https://doi.org/10.48550/arXiv.2603.27211 (Accessed 28 March 2026).
37. Z. Zhu *et al.*, Data for Evidence of intertwined pair density and charge density wave orders in UTe2. Zenodo. https://doi.org/10.5281/zenodo.21109271. Deposited 1 July, 2026.